

UCLA

UCLA Previously Published Works

Title

Oxidation Dynamics of Supported Catalytic Cu Clusters: Coupling to Fluxionality

Permalink

<https://escholarship.org/uc/item/3b36x6pg>

Journal

ACS Catalysis, 12(1)

ISSN

2155-5435

Authors

Guo, Han
Poths, Patricia
Sautet, Philippe
et al.

Publication Date

2022-01-07

DOI

10.1021/acscatal.1c04100

Peer reviewed

Oxidation Dynamics of Supported Catalytic Cu Clusters: Coupling to Fluxionality

Han Guo^[a], Patricia Poths^[a], Philippe Sautet^{[a,b,c]}, and Anastassia N. Alexandrova^{*[a,c]}*

[a] Department of Chemistry and Biochemistry, University of California, Los Angeles, Los Angeles, CA 90095-1569 (USA)

[b] Department of Chemical and Biomolecular Engineering, University of California, Los Angeles, Los Angeles, CA 90095-1569 (USA)

[c] California NanoSystems Institute, Los Angeles, CA 90095 (USA)

AUTHOR INFORMATION

Corresponding Authors

Anastassia N. Alexandrova – Email address: ana@chem.ucla.edu

Philippe Sautet – Email address: sautet@ucla.edu

ABSTRACT Copper oxide nanoclusters have a wide range of catalytic applications, such as the selective oxidation of hydrocarbons. O₂ binding to the catalyst, activation, and release upon reagent oxidation are key events in these catalytic chemistries. These events are expected to be accompanied by significant structural changes of the Cu clusters, because O atoms integrate into the cluster, rather than bind to its surface. Topping the complexity of the problem, partially oxidized Cu clusters are known to exhibit strong fluxionality, and feature diverse and interconverting structures and oxygen contents in conditions of oxidative dehydrogenation (ODH). Hence, a significant dynamic coupling between the ‘hot’ O₂ molecule impacting the cluster at reaction temperatures and the cluster fluxionality can be expected. In this work, we focus on the dynamics of dioxygen integration into a partially oxidized Cu cluster supported on hydroxylated amorphous alumina – a system recently reported to be an exceptionally selective catalyst for cyclohexane ODH with very little CO produced, whose mechanistic underpinnings are of utmost interest. The statistics over a swarm of adsorption and scattering trajectories where O₂ hits various sites on the cluster at reaction temperature shows that the O₂ binding does not only follow the minimal energy paths. O₂ also rarely integrates into the cluster in a single step, and instead first binds to a single Cu atom via either η^1 -O₂ or η^2 -O₂ mode. Surprisingly, this step often has higher barrier than the subsequent O₂ integration and dissociation, which in turn take multiple steps and complete the oxidation process. Dynamic trajectories starting from the key transition state of integration of the adsorbed O₂ can also lead to different intermediate structures during or right after the dissociation, due to the energy released from the transition state and the thermal intra-cluster effects. From these activated O₂ chemisorbed structures, O₂ dissociation occurs with moderate barriers (~0.5 eV), producing multiple final oxidized Cu₄O₄ states. Hence, a diversity of reaction profiles for the attack of supported Cu cluster by O₂ emerges due to the dynamic effects, with implications for mechanisms, kinetic models, and catalyst design principles.

KEYWORDS

Oxidation catalysis, cluster fluxionality, ab initio molecular dynamics, supported clusters

Introduction

Selective oxidation is a major catalytic reaction for the conversion of hydrocarbons into valuable compounds. In this class, oxidative dehydrogenation (ODH) appears a key reaction to valorize alkanes, overcoming the thermodynamic limitation of direct dehydrogenation. Reducible oxides as V_2O_5 , MoO_3 , Co_3O_4 and recently CuO are used as catalysts.¹⁻⁴ The reaction is structure sensitive, both for its activity and selectivity to alkene, so that the size and shape of the catalytic particles and the nature of the support are important.

Sub-nano metal clusters have received considerable attention in heterogeneous catalysis due to their remarkable and tunable catalytic activities. Sub-nano clusters can provide solvent-free aerobic oxidative transformation and a large number of active sites due to their small sizes. Among different metal clusters, copper has gained growing interest, due to its low toxicity and cost. Copper oxide nanoclusters have a wide range of catalytic applications, such as already mentioned selective oxidation of hydrocarbons,⁵ as well as reduction of nitrogen oxides,⁶ and reduction of carbon dioxide⁷, due to the varying oxidation states of Cu. Vajda et al. reported partially-oxidized Cu and Pd clusters as catalysts for the ODH of cyclohexane to cyclohexene and benzene.⁸ They found that Cu oxide cluster has the highest selectivity towards the desirable cyclohexene, and is more selective than bulk Cu oxide catalysts. Riisager et al. synthesized CuO nanoparticle catalysts for the oxidation of benzyl alcohol to benzaldehyde with excellent selectivity under aerobic conditions.⁹

However, cluster structural diversity and fluxionality make them extremely complex, obfuscating the experimental characterization and computational modeling. Recent studies show that a large number of metastable isomers are thermodynamically accessible under realistic catalytic reaction conditions, and in some cases metastable structures are predicted to be more catalytically active than the lowest-energy structure (the global minimum, GM).¹⁰⁻¹⁹ Thus, a cluster catalyst should be represented by a statistical ensemble of many thermodynamically-accessible structures, instead of a single structure, and multiple reaction pathways jointly represent the catalytic mechanism. Cluster isomers can interconvert before or during catalytic reactions due to thermal effects or induced by adsorption of small molecules. The rearrangement of the cluster could couple with the reaction coordinate, depending on the relative timescales of the cluster fluxionality and the reaction. Thus, the thermodynamic study of the minimum energy path (MEP) alone may not describe the catalytic activity appropriately.

In this study, we explore the adsorption and dissociation of O_2 on the Cu_4O_2 cluster deposited on amorphous alumina using both static thermodynamic methods and *ab initio* molecular dynamics (AIMD) simulations²⁰. A previous theoretical study used the grand canonical basin hopping method to show the presence of a wide range of low free energy Cu_4O_x structures with various O content (from 2 to 5) under realistic catalytic conditions ($T = 473$ K, $pO_2 = 0.5$ bar).¹² Of all the accessible cluster compositions and their relative affinities to dioxygen, the oxidation of Cu_4O_2 with O_2 appears to play an important role in the most promising catalytic cycle of oxidation reactions, being involved in the regeneration of the catalyst structure after the hydrocarbon oxidation. In previous studies, the adsorption and dissociation of O_2 on copper clusters^{21–24} and copper/copper oxide surfaces^{25–30} has been investigated experimentally and theoretically. However, the potential energy landscape and dynamics of O_2 adsorption and dissociation on copper oxide clusters has not been directly addressed. In this work, we compare the MEPs and the molecular dynamics simulations on different reaction sites. The *ab initio* MD and quasi-classical trajectory, AIMD-QCT, approach,^{31–37} with vibrational zero-point energy (ZPE) imparted to the molecule, is used to simulate O_2 impinging on the cluster and forming an intermediate along the path of O_2 dissociation. Calculations of the subsequent steps of O_2 integration and dissociation, their mechanistic bifurcation, and energetics complete this work.

Methods

The GM structure of Cu_4O_2 deposited on a periodic model of the amorphous alumina support (Figure 1a), reported in a previous study,^{12,38} is chosen as the model system. Since our dynamics study focuses on the local region of the catalyst containing a deposited Cu_4O_2 cluster, reducing the computational expense was possible by using a cluster model (Figure 1b). It consists of the Cu_4O_2 cluster and a portion of the support containing a sufficient number of O and Al atoms, i.e. 19 O atoms and 6 Al atoms. The truncated surface terminates with O atoms, whose previously bonded Al atoms are replaced by H atoms. We use potentials with partial valency for some terminal H to neutralize the system. The terminal H are relaxed first, with other atoms staying at their original positions. During the dynamics simulations and reaction paths searching, all the atoms, except the terminal O and H, are allowed to move.

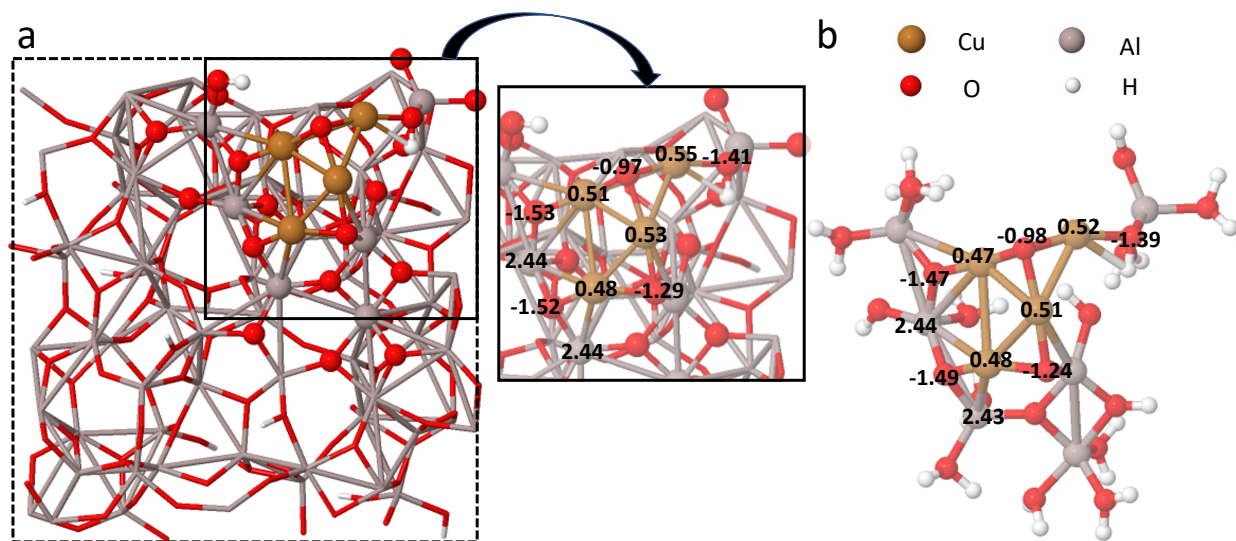


Figure 1. (a) Optimized structure for Cu_4O_2 deposited on a periodic model of the amorphous alumina support (top view), with unit cell boundary shown as dashed lines, and atomic Bader charges on Cu_4O_2 and nearby atoms. (b) Optimized cluster model for Cu_4O_2 deposited on the amorphous alumina support, which is modeled by 19 O atoms (4 moving O) and 6 Al atoms. Atomic Bader charges on Cu_4O_2 and nearby atoms are shown for comparison with the full model in (a).

We benchmark the cluster model against the original periodic system. The bond lengths and atomic charges of the cluster model are very close to those of the full system, with differences in bond length less than 0.16 Å and charge differences less than 0.06 e, indicating similar chemical bonding and reactivity (Figures 1a, 1b, S1). The model adequacy is further confirmed by the same electron density on its highest occupied molecular orbital (HOMO) and lowest unoccupied molecular orbital (LUMO) as in the original system (Figure S1).

In this study, electronic structure calculations and AIMD simulations are carried out using the DFT-based Vienna ab initio simulation package (VASP).^{39–43} The projector augmented-wave (PAW) potentials are used to describe the interactions between the ionic cores and the electrons^{39,44}, and the one electron functions are developed on a basis set of plane-waves with a cutoff energy of 400 eV for O_2 adsorption dynamics and 450 eV for MEPs and O_2 integration dynamics. The exchange-correlation effects are treated using the Perdew-Burke-Ernzerhof (PBE) functional.⁴⁵ To take into account the strong self-interaction of the Cu d electrons, the Hubbard model⁴⁶ with $U = 2.0$ eV for the d orbitals of Cu is used, which is benchmarked in the previous study.¹² The spin-

polarized calculations are employed to treat spin multiplicities. The dimensions of the unit cell are 20Å x 20Å x 25Å, and the separation between periodic images is larger than 9 Å, which is sufficient to prevent their interaction. A 1×1×1 Monkhorst-Pack k -point grid centered at the Γ -point is used in all calculations, and the convergence criterion for the SCF is set to 10⁻⁶ eV for MEP search and 10⁻⁵ eV for AIMD simulations. The transition states and reaction paths are located using the climbing image nudged elastic band (CI-NEB) method,^{47,48} and the calculations are considered converged when the residual forces are less than 0.02 eV/atom.

The AIMD calculations²⁰ are performed in an NVE ensemble. The AIMD-QCT approach,³¹⁻³⁷ with vibrational zero-point energy (ZPE) imparted to the molecules, is used to simulate O₂ impinging on the cluster and forming an intermediate along the path of O₂ dissociation.

Minimum Energy Paths for O₂ Adsorption and Dissociation

To study the adsorption and dissociation of O₂ on Cu₄O₂/Al₂O₃, we first located the MEPs on different reaction sites. Figure 2 shows the lowest-barrier path (also recomputed on the full slab, to support the validity of the cluster model – Figure S2a, as well as a free energy profile – Figure S2b), which consists of multiple steps. The O₂ molecule will first bind to a single Cu atom via one or two O atoms, to form either a η^1 -O₂ or a η^2 -O₂ binding mode (Figure S3). The Cu-O bond length is 1.9 - 2.1 Å depending on the Cu site, and the O-O bond is elongated by 0.04 - 0.07 Å compared to the gas-phase molecule. The adsorption energies for the four Cu sites are slightly different within the range of -0.21 eV to -0.43 eV. We note that the adsorption of O₂ causes structural change in the Cu₄O₂ cluster by pulling the binding Cu atom out of the cluster up by 0.17 - 0.58 Å. The onset of this structural change is rather late, when O₂ is only 3.0 - 3.5 Å away from the adsorption site. Thus, from the study of the PES, it is unclear whether or not the cluster would be able to relax to the MEPs during dynamics simulations.

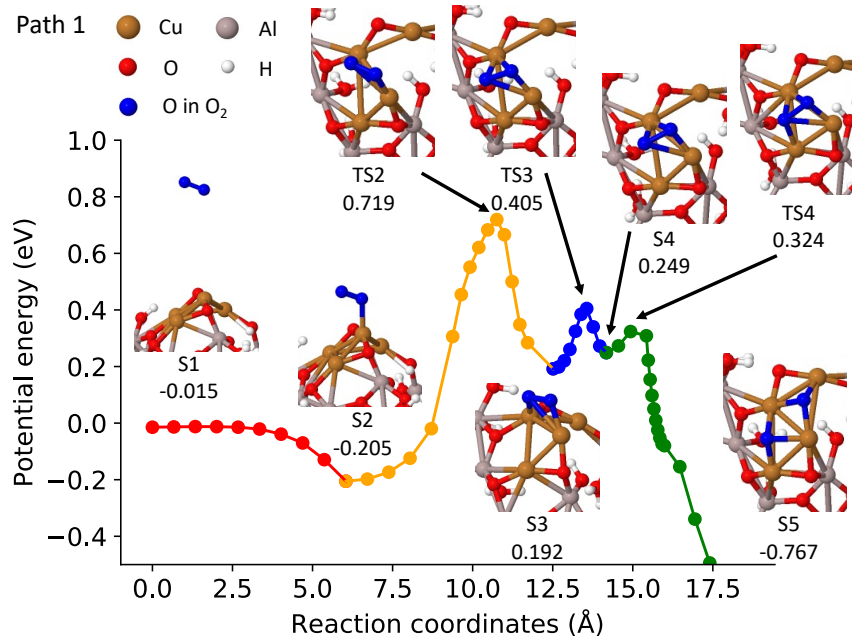


Figure 2. Lowest-barrier minimum energy path (Path 1) and optimized structures (‘S’ represents a local minimum, and ‘TS’ represents a transition state) along the path for O₂ adsorption and dissociation on Cu₄O₂/Al₂O₃. The reaction coordinate is defined as the geometry difference between two structures given by $(ds)^2 = \sum_{n=1}^{18} \sum_{i=1}^3 (dx_{ni})^2$, where x_{ni} is the i^{th} Cartesian coordinate of atom n , and the reaction coordinate is set to zero at the initial asymptotic geometry. The energy of each structure relative to the asymptotic structure is also shown.

It is known that O₂ is likely to dissociate over a Cu-Cu bond, so we investigated the dissociation over four different Cu-Cu bonds. On three of the four MEPs, we found another two intermediates before O₂ dissociation, as shown in Figures 2, S3b and S3c. In the first one (state S3), O₂ adopts a $\mu\text{-}\eta^1\text{:}\eta^1\text{-O}_2$ binding geometry, in which each O atom binds to one of two adjacent Cu atoms and the O-O bond is almost parallel to the Cu-Cu bond. This state is triplet with spin density localized on O and adjacent Cu atoms. The O-O bond length is increased to 1.31 - 1.38 Å, depending on the path, which is 0.02 - 0.11 Å longer than that in state S2. We note that state S3 with $\mu\text{-}\eta^1\text{:}\eta^1\text{-O}_2$ is energetically less stable than state S2, with positive adsorption energies on path 1 (Figure 2) and path 3 (Figure S4). This remains the case even on the free energy pathway, where the S2 state is destabilized due to the entropy loss of O₂ binding. On path 1, the formation of S3 is the rate limiting step, with a barrier of 0.92 eV relative to nominal intermediate state S2, and 0.719 eV relative to the initial asymptotic geometry. This relatively high barrier is due to the cleavage of a Cu1-Cu3 bond. The other intermediate (state S4) forms, depending on the path, either a $\mu\text{-}\eta^1\text{:}\eta^2\text{-}$

O_2 or $\mu\text{-}\eta^2\text{:}\eta^2\text{-}O_2$ binding mode, in which the O-O bond is skew or perpendicular to a Cu-Cu bond. Different from state S3, the multiplicity for this state is singlet. O_2 is further activated with the O-O bond elongated to 1.42 - 1.44 Å. The formation of S4 is endothermic with a barrier of 0.21 - 0.60 eV. The last step is O_2 dissociation, and its barrier can be very different depending on the paths: from 0.07 (path 1, Figure 2) to 1.19 eV for path 2 (Figure S4). We note that the rate-limiting step varies for different sites, but might be associated with cluster restructuring upon O_2 attachment rather than O_2 dissociation, at least from the MEP of path 1. All steps tend to involve Cu_4O_2 isomerization. The formation of the $\mu\text{-}\eta^1\text{:}\eta^2\text{-}O_2$ or $\mu\text{-}\eta^2\text{:}\eta^2\text{-}O_2$ species and the dissociation of O_2 (discussed in more detail below) may involve spin flipping. In some cases, the intersystem crossing point appears to be very close to the TSs, rendering the DFT treatment imperfect. These effects will not alter our ultimate conclusions, since the TSs in question are not rate-limiting.

Dynamics of the O_2 attack

However, it is dubious that the MEPs would provide an appropriate description of the reaction, given a variety of initial cluster structures that are thermodynamically accessible, the large momentum carried by the incoming O_2 molecule, and the relative timescales of the reaction and of the cluster isomerization being presumably close. To study the cluster structural changes during the course of the reaction, we employed AIMD simulations on O_2 adsorption and the formation of $\mu\text{-}\eta^1\text{:}\eta^1\text{-}O_2$ binding structure in Path 1 which involves a Cu-Cu bond breaking.

For the O_2 adsorption, the AIMD simulations are performed at cluster temperatures of 400 K and 700 K. The initial conditions for the cluster (velocities and displacements from the equilibrium structure) are sampled from an equilibrated configuration pool. More details can be found in the supporting information. The O_2 molecule is initially placed 6.5 Å above the cluster, where the interaction with the cluster is weak, and the horizontal position (X, Y coordinates) is randomly sampled within a rectangular region, whose boundary is 1.5 Å away from the cluster. Given the high vibrational energy of the stretching mode, we only consider O_2 initially in the vibrational ground state, with ZPE imparted to it. The incident translational energy is set to 0.19 eV, corresponding to a velocity pointing downward of 0.01 Å/fs. 128 production runs are performed for 1 ps with a time step of 0.5 fs. The simulation time is chosen so that the $\eta^1\text{-}O_2$ or a $\eta^2\text{-}O_2$ state is formed or the molecule is scattered back for most trajectories. Due to the relatively short simulation time, the dissipation of energy into the support may not be sufficient. Note that the

number of AIMD trajectories used in this study is relatively small, so the calculated adsorption probability will have a relatively large standard error. However, the focus of this study is not to have a quantitative prediction but a qualitative investigation of dynamic coupling. At the end of the trajectories, we observed two outcomes: adsorption and scattering. O_2 is considered scattered if it moves away from the cluster and is at least 3.0 Å away from the impact site at the end of the trajectory. For adsorption trajectories, O_2 is considered to have adsorbed on the cluster when the Cu-O distance reaches 2.2 Å.

Given the initial velocity, it takes ca. 400 fs for O_2 to arrive to the cluster. As O_2 approaches, the cluster fluxionality is appreciable, which can be measured by the Root-Mean-Square displacement (RMSD) between the structure at time t and the equilibrium structure. Before the O_2 adsorption event, the calculated RMSD in Cu_4O_2 is 0.20 - 0.25 Å at 400 K, and 0.25 - 0.30 Å at 700 K. However, these structural changes contain both the O_2 -induced and the intrinsic thermal cluster fluctuations. In order to distinguish between them, we perform the same number (128) of reference runs with O_2 removed, while the initial conditions of Cu_4O_2 and the support remaining the same as in the production runs. The O_2 -induced cluster fluxionality can be quantified by the structural divergence of a production trajectory from its reference trajectory, defined by the RMSD between the two trajectories. The typical adsorption and scattering trajectories thus visualized relative to the thermal dynamics of the cluster alone are shown in Figure 3a and 3c. The trajectory can be viewed as consisting of three stages, which can be discussed separately: (i) O_2 -induced cluster dynamics during the O_2 approach, (ii) cluster dynamics coupling to O_2 binding or scattering, and (iii) cluster dynamics following the O_2 binding or scattering due to nuclear momentum exchange upon collision and/or electronic changes. These stages are marked by vertical dashed lines in Figure 3.

When O_2 approaches the cluster and before it reaches a distance of 4.0 Å from Cu (the first vertical dashed line from the left in Figure 3), in both adsorption and scattering, the effect of O_2 on the cluster dynamics is minor. The divergence is 0.012 ± 0.003 Å and 0.018 ± 0.012 Å, at cluster temperatures of 400 K and 700 K, respectively (Figure S5). This oxygen-induced cluster dynamics is an order of magnitude weaker than the native thermal fluxionality of Cu_4O_2 , because the interaction between O_2 and the cluster at such distances is weak (as also seen in the MEPs). Therefore, when O_2 approaches the cluster, the majority of the cluster fluxionality is driven by

thermal effects. In addition, the vibrational motion of O_2 retains its gas-phase behavior and does not couple to the cluster (Figure 3b and 3d).

The interaction starts to increase at a O_2 -Cu distance of 3.0 - 3.5 Å. At distance below 3 Å (second from the left vertical line in Figure 3) the O_2 -induced dynamics becomes apparent (Figure 3a, 3c and Figure S6). For most trajectories the largest O_2 -induced structural change is related to the impact Cu atom being pulled out of the cluster (purple line in Figure 3a), which is consistent with the change on the MEPs. However, the O_2 -induced cluster fluxionality is still limited when O_2 arrives at the impact site.

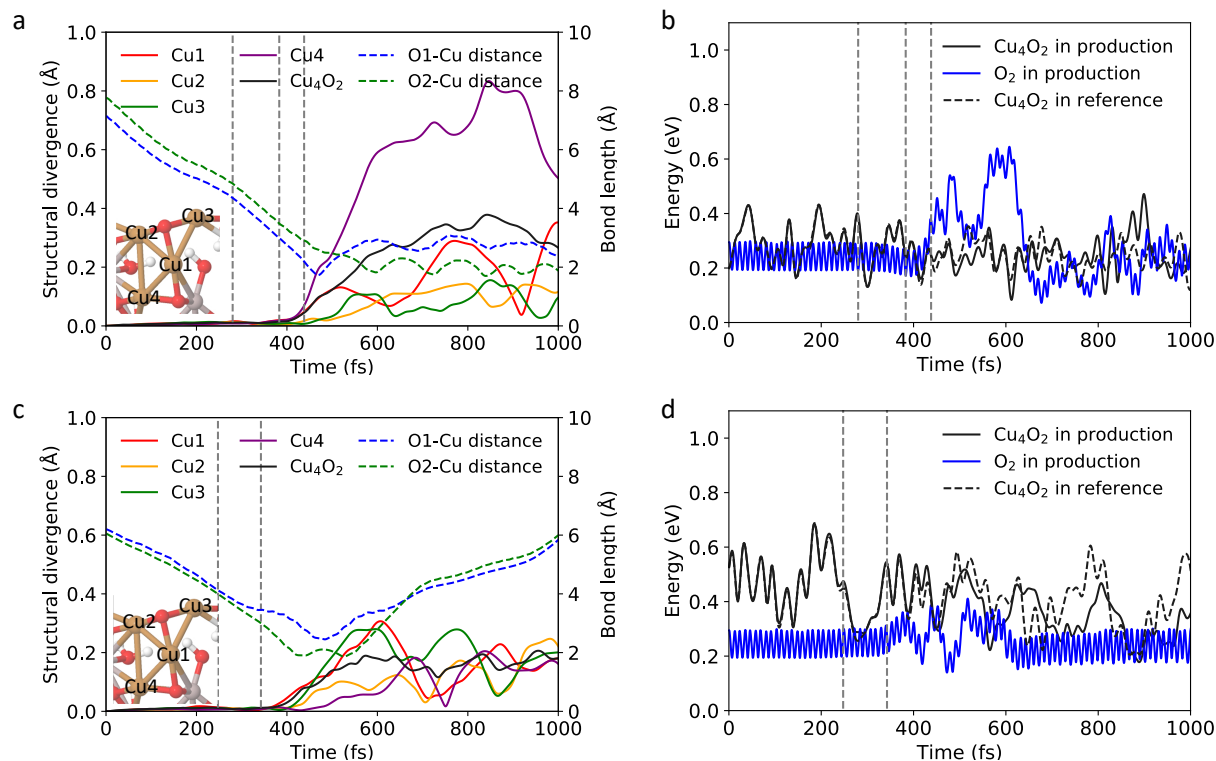


Figure 3. Typical structural divergences between production trajectories and their reference trajectories for (a,c), and the evolution of the kinetic energies in Cu_4O_2 and O_2 (b,d), in an adsorption case (impact site: Cu4) – top row, and a scattering case (impact site: Cu1) – bottom row. Both are plotted at 400 K. In (a,c) the dashed blue and green lines represent the distance between O_2 and the impact atoms. In (b,d), the solid black and blue lines represent kinetic energies in Cu_4O_2 and O_2 for the production trajectories, and the dashed lines represent energies in Cu_4O_2 for the corresponding reference trajectories without O_2 . The vertical dashed lines in all panels mark the times when the distance between O_2 and the impact Cu site reaches 4.0 Å, 3.0 Å, and O_2 adsorption.

For adsorption trajectories, it only takes 85 fs on average for the O₂-Cu distance to reduce from 3.0 Å to 2.2 Å. During this short period of time, the average structural divergences increase to 0.062 ± 0.031 Å at 400 K and 0.072 ± 0.037 Å at 700 K. The O₂-induced dynamics becomes most obvious in the timeframe after O₂ adsorption (to the right of the third dashed line in Figure 3a and 3b). Here we have energy transfer from O₂ to the cluster causing the reshaping of the Cu₄O₂ core, and the vibrational mode of O₂ mixing with the cluster's modes affecting cluster dynamics (Figure 3b). The whole O₂-adsorbed Cu₄O₂ system eventually relaxes to a lower-energy adsorbed state. A variety of adsorbed minima are produced upon the dynamic O₂ attachment (Figure 4) - a substantially richer reactivity picture than the MEPs. Note that these structures differ mainly in the configurations of the bound O₂, which, however, can impact the outcome of the subsequent step of O₂ integration into the cluster. In this study, we only explore the dynamics with a certain amount of incident transitional energy imported into O₂. With different incident translational energy, we expect different amount of energy transferring into the cluster, accordingly, leading to different degree of cluster fluxionality.

Part of the incident energy will eventually dissipate into the support. As shown in Figure S10 (a), in the adsorption trajectory the plot of kinetic energy in the support starts to diverge from that in the reference trajectory at about 550 fs, about 50 - 100 fs latter than the O₂-induced cluster change, indicating the transfer of incident energy into the support. This can also be seen in the comparison between the support average RMSD of adsorption trajectories and reference trajectories without O₂: the average RMSD in the cluster starts to increase at 350 fs, while the support average RMSD starts to increase at 400 fs. We also note that the average RMSD in the support is small compared to that in the cluster (Figure S6), and the support RMSD reaches equilibrium within the 1000 fs. However, given the small size of our model and relatively short simulation time, the energy dissipation may not be sufficient in our simulation.

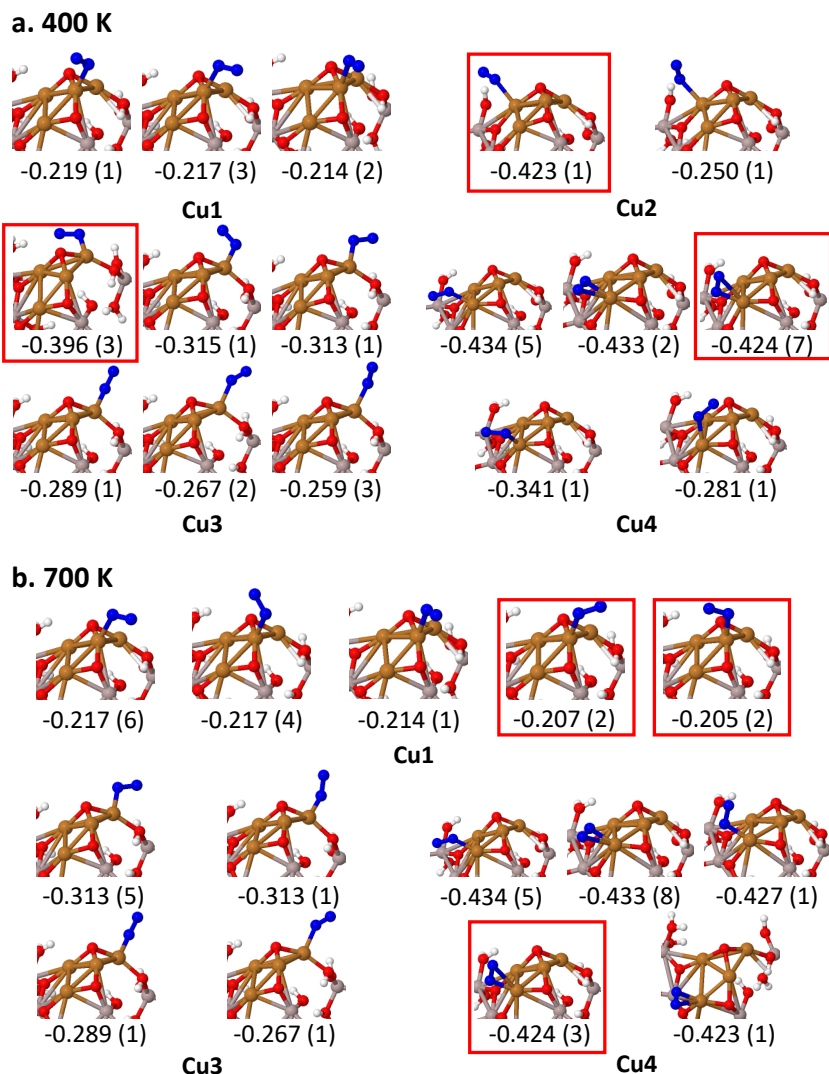


Figure 4. Unique products of O_2 attachment seen in the dynamics at (a) 400 K and (b) 700 K, obtained by optimizing the final structure from each adsorption trajectory to the nearest local minimum. Structures are grouped by the Cu atom on which adsorption occurs. The minima that are seen on the MEPs in Figures 2, S2,S3 are outlined in a red box. The energy of the isomer and the number of trajectories producing that isomer (in parentheses) are also shown.

In most of the scattering trajectories, O_2 either immediately leaves the strong O_2 -Cu interaction region, where the O_2 -Cu distance is less than 3.0 \AA , within 350 fs, or does not enter this region. The scattering trajectories are affected just by the energy exchange of the cluster with O_2 upon collision, causing the changes of atomic velocities in the cluster, but featuring smaller divergences that eventually diminish after O_2 leaves the cluster surface (Figure S5). The average structural divergences at the shortest O_2 -Cu distances are: $0.073 \pm 0.041 \text{ \AA}$ at 400 K, and $0.105 \pm 0.057 \text{ \AA}$

at 700 K. In some scattering trajectories, O_2 adsorbs first and then desorbs from the cluster. In this case, the O_2 -induced structural changes are slightly greater (0.150 ± 0.076 Å at 400 K, and 0.167 ± 0.135 Å at 700 K), due to the longer interaction times. No scattering trajectories result in complete cluster isomerization to new minima.

In Figure 5, we plot the top view of O_2 impact sites, defined as the position of O_2 when it adsorbs on Cu_4O_2 (O_2 -Cu distance first reaches 2.2 Å), or when the O_2 -Cu distance is shortest if it never reaches 2.2 Å. The adsorption probabilities of O_2 on different Cu sites are shown in Table 1. When computing the adsorption probability, we ignore the trajectories where O_2 lands on the support rather than the cluster (i.e. where the distance between O_2 and any Cu atom is larger than 2.2 Å).

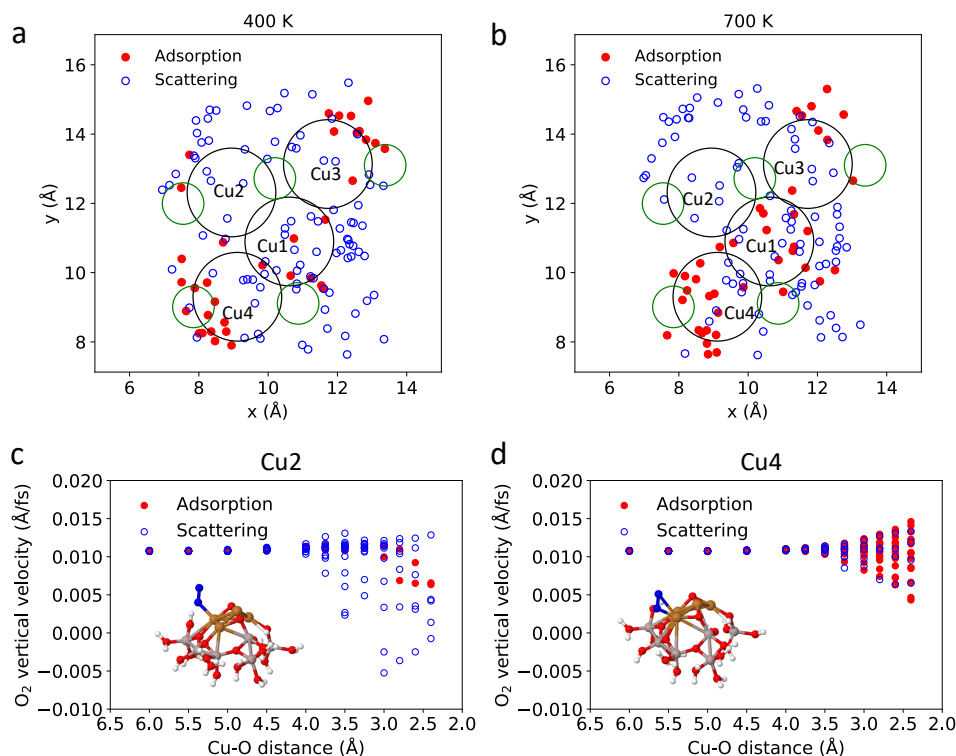


Figure 5. (a) (b) Top view of O_2 impact sites, defined as the position of O in O_2 when the Cu-O distance first reaches 2.2 Å or when the Cu-O distance is shortest if it never reaches 2.2 Å. Results are shown for adsorption trajectories (red points) and scattering trajectories (void blue circles) at (a) 400 K and (b) 700 K. The void black and green circles represent the Cu and O atoms in Cu_4O_2 . (c) (d) Vertical velocity of O_2 in each trajectory along the path (positive values indicate that O_2 is moving towards the cluster); results are shown for collisions on (c) Cu2 (the more likely scattering site) and (d) Cu4 (the more likely adsorption site).

Table 1. Adsorption probability with statistical error for each impact Cu atom and the total adsorption probability at the cluster temperatures of 400 K and 700 K.

Cu impact site	400 K	700 K
Cu1	$14 \pm 5.4 \%$	$25 \pm 6.1 \%$
Cu2	$12 \pm 7.8 \%$	$0 \pm 0.0 \%$
Cu3	$39 \pm 9.2 \%$	$42 \pm 10.1 \%$
Cu4	$70 \pm 9.6 \%$	$83 \pm 7.9 \%$
Total	$32 \pm 4.4 \%$	$37 \pm 4.6 \%$

We note that, although the Cu2 and Cu4 sites have similar O₂ adsorption energies, close to -0.4 eV and ~0 eV barrier height, for their most stable adsorbed states (Figure S3), the adsorption probability on Cu4 is much higher than that for Cu2. This can be rationalized by the ‘sudden’ behavior of O₂ adsorption, i.e. the reaction occurs rapidly without gradually relaxing to the MEPs. Given the relatively small O₂-induced cluster fluxionality, most trajectories do not follow the MEPs towards the most stable adsorbed states (Figure 5c, 5d and S7). Despite similar energy profiles along the MEPs, the two Cu atoms may have different energies for the paths leading to metastable and unstable states. In order to study this effect, we plot the O₂ vertical velocity for collisions on different Cu atoms in Figure 5c and 5d and S6, in which the positive value indicates O₂ moving towards the cluster while the negative value indicates O₂ scattering away from the cluster at different O₂-Cu distances. Initially, all the O₂ molecules have the same velocity towards the cluster, and the decrease/increase in the velocity is due the repulsive/attractive interaction between O₂ and the cluster. We find that the vertical velocity of O₂ starts to decrease early at an O₂-Cu distance of 4.0 Å over the Cu2 site (Figure 5c), and in some trajectories O₂ reaches the turning point and scatters before 3.3 Å. This indicates relatively small attraction, or even repulsion between the cluster and O₂ when O₂ is close to the Cu2 site in these trajectories starting from the meta-stable and unstable structures. In other words, the energy on the PES increases rapidly when the cluster is displaced from its structure in the lowest energy adsorbed state, leading to relatively

high barriers for O₂ adsorption. Thus, most O₂ are scattered on the Cu2 site. However, on the Cu4 site (Figure 5d) the O₂ vertical velocity is only barely decreased or even increased at an O₂-Cu distance of 3.5 Å, suggesting a relatively flat PES upon associated cluster structural change, consistent with the observation in the dynamics simulations. The cluster appears more flexible in this area. Therefore, the dynamics simulation provides a more appropriate description on the site activity than the MEP study, since it includes the contribution of meta-stable and unstable states, and shows clear differences in sticking coefficients on different Cu sites.

Finally, we notice that the adsorption probability is larger at a higher cluster temperature, especially at the Cu1 and Cu4 sites (Table 1). The reason for this temperature effect is that at 700 K Cu₄O₂ accesses configurations further from equilibrium, some of which have higher adsorption energies. Indeed, as shown in Figure S8, structures with greater RMSD feature the greatest adsorption probabilities, particularly the structures within larger RMSD in the range of 0.34 - 0.42 Å, accessible only at 700 K.

Dynamics of the O₂ integration into the cluster

O₂ incorporation into the cluster is accompanied by cluster reorganization on MEP and corresponds to descending from the highest TS on the MEP in Path 1, creating a metastable non-dissociated O₂ structure (S3 on Figure 2), the precursor to the O-O dissociation. Hence, we may expect possible further dynamic coupling between this reaction step and the cluster motion. However, it is likely to be considerably less dramatic compared to the first step of O₂ attack, since now there is no new input of kinetic energy. AIMD simulations were performed on the representative process of the formation of this $\mu\text{-}\eta^1\text{:}\eta^1\text{-O}_2$ species in Path 1 (Figure 2), which involves the cleavage of a Cu-Cu bond. The purpose of this simulation is not to exhaust all possible reaction paths from state S2 or all intermediates preceding deeper O₂ integration, but to gain a qualitative insight into the degree of possible dynamic coupling for this process, compared to the MEP. The simulations start from the transition state TS2 in Figure 2 (rate-limiting for this MEP), propagating in backward to the reactant (states S1 and S2), and forward to the product (state S3). The initial vibrational states of TS2 are sampled from the Boltzmann distribution at 400 K.^{49–52} An independent harmonic oscillator model with random phase is used to generate the initial velocities and displacements from the transition state. Corrections are made for modes with large anharmonicities using the correct anharmonic potential energy surfaces calculated using the DFT

(see SI for details). The translational energy of the reaction coordinate samples a classical Boltzmann distribution. We performed 20 simulations for 0.5 ps along each direction, with a time step of 0.5 fs.

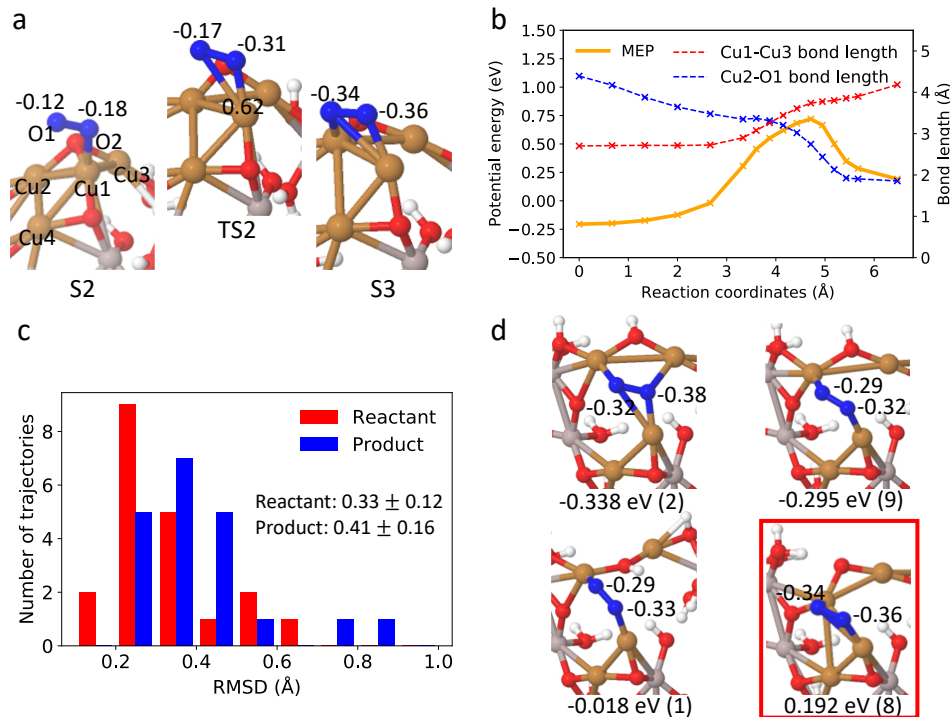


Figure 6. (a) Optimized geometries for the reactant (S2), transition state (TS2) and product state (S3) from the MEP of step 2 in Path 1. The atomic charges on O₂ from Bader charge analysis are also shown. (b) MEP (solid line) and the Cu1-Cu3 and Cu2-O1 bond lengths along the path (dashed lines). (c) Distributions of the cluster RMSDs in the reactant and product structures relative to the S2 and S3 equilibrium structures, respectively. (d) Optimized product geometries and atomic charges on O₂ obtained from Bader charge analysis. The structures are extracted at 500 fs of the forward trajectories and relaxed to the nearest minima. The minimum that is seen on the MEP (state S3) is highlighted. The energy of the isomer and the number of trajectories producing that isomer (in parentheses) are also shown.

On the MEP, the largest structural changes in Cu₄O₂ during this step are the formation of the Cu2-O1 bond and the cleavage of the Cu1-Cu3 bond (Figure 6b). We note that these two bonds' lengths change concurrently in the AIMD trajectories. For trajectories propagating to the reactant state, the formation of the reactant from TS2 (i.e. the Cu1-Cu3 bond reaching the equilibrium bond length of 2.7 Å in state S2, Figure 6a and 6b) takes on average 283.9 fs. Figure 6c shows the distributions of the cluster RMSDs in the reactant (red) and product (blue) structures, extracted at 500 fs of the trajectories, relative to the S2 and S3 states, respectively. The trajectory-averaged

cluster RMSD in the reactant structures is slightly larger than that of the TS structures from which the trajectories were launched. From the trajectories going backward from TS2, we optimized the final geometries to the nearest minima. Interestingly, 8 out of 20 trajectories go back to S1 where O_2 is detached from the cluster, with the Cu-O distance larger than 3 Å. After geometry optimization, five of these structures relaxed to the gas-phase molecule and the bare cluster, as the energy released from the TS supplies sufficient kinetic energy to overcome the desorption barrier. This implies that TS2 can be reached dynamically directly from the gas phase O_2 , bypassing S2 and therefore decreasing the overall costly barrier, contrary to what is seen from the MEP. This is perhaps not unexpected from looking at the free energy profile (Fig. S2b), where the S2 state is destabilized and rendered no longer a local minimum on the MEP due to the loss of entropy upon binding the O_2 molecule. In the remaining trajectories the system forms different stable adsorption states with either η^1-O_2 or η^2-O_2 binding mode.

For trajectories going forward, towards the product state, S3, the average time to form the Cu2-O1 bond (i.e. reaching the equilibrium Cu2-O1 bond length of 1.9 Å) is 131.5 fs. As shown in Figure 6c (blue), the RMSD distribution of the product state shifts to higher values compared to the reactant and the initial TS2, indicating more diverse cluster structures. The product structures, extracted at 500 fs and relaxed yield four isomers shown in Figure 6d, one of which is S3 and the other three being more stable than S3 by up to 0.5 eV. Note that only 8 out of the 20 trajectories follow the MEP and produce the S3 state. In all other final states, we observe the cleavage of the Cu1-Cu2 and Cu2-Cu4 bonds, which apparently have been weakened by the formation of the Cu-O σ bonds. These product states would not be found in pure MEP calculations. The reason they are found in the dynamics is probably that the energy released from the TS, combined with the cluster thermal effects, is sufficient to break these weakened Cu-Cu bonds, and assist cluster isomerization in the course of the dissociation and right after the dissociation. Therefore, although starting from the same TS, the reaction may lead to different product structures in the dynamics, which will complicate the reaction network by opening up new reaction paths, and producing new intermediates or product states.

None of trajectories started from TS2 resulted in O-O bond breaking. This final step can start from the four different product structures in Figure 6d. The corresponding MEPs for O_2 dissociation are shown in Figure S9. The barriers to dissociation range from 0.4 to 0.8 eV, and are the lowest (0.4 to 0.6 eV) for the two alternative paths that start from the same lowest-energy

product state in Figure 6d (Figure S9a,b, Note S1). These two profiles are exothermic, and yield products that are close in stability to S8 (Figure 2). Starting from the second lowest energy product state from Figure 6d, the barrier to dissociation is slightly higher (0.65 eV, Figure S9c), and the process is endothermic. However, this barrier remains below that of TS2. The only O₂ dissociation that has a barrier surpassing that of TS2 starts from the third lowest energy product in Figure 6d (which is nonetheless more stable than S3 in Figure 2). Due to its higher energy, we would expect this path to be followed less preferentially. On all paths, the O-O bond dissociation involves significant Cu core rearrangement, indicating that the cluster continues to be most fluxional during the process of O₂ incorporation. Overall, these results illustrate how every MEP of O₂ attachment to the supported Cu₄O₂ cluster can correspond to a myriad of mechanistic possibilities when dynamics is considered. Therefore, the overall cluster oxidation kinetics has to be incredibly complicated. Also, our findings suggest that O-O bond breaking can be energetically less costly than the initial O₂ binding to the cluster and the accompanying cluster rearrangement – a counterintuitive result.

Conclusions

In this study, we locate the MEPs and perform the molecular dynamics simulations for the adsorption and integration of O₂ to the Cu₄O₂ cluster deposited on an amorphous alumina support. This process plays a key role in oxidation catalysis by supported Cu₄ clusters, as it is the most viable path to catalyst regeneration.¹² The comparison between the static MEPs and the dynamical trajectories uncovers a rich dynamic picture of nano cluster catalysis, hidden if just MEPs are considered, and quite contrasting to what is possible on extended metal surfaces. The dynamics of O₂ adsorption to form the $\mu\text{-}\eta^1\text{:}\eta^1\text{-O}_2$ species induces only minor cluster rearrangements, but produces a wide variety of conformations, most of which are not seen on the MEP. Surprisingly, the step of O₂ adsorption to the cluster, can be most energetically costly. The subsequent O₂ integration into the cluster takes place with somewhat less dramatic dynamic effects, but with substantial cluster core reorganizations. The motion of Cu₄O₂ mixes with the O₂ motion. The energy released from the TS associated with O₂ integration and the thermal vibrational excitations can promote the cluster core isomerization, again producing a variety of different intermediates not seen on the MEPs. This effect is attributed to cluster fluxionality, easily triggered both thermally, and by interactions with reagents in reaction conditions. The final O₂ dissociation can

follow several different paths, producing multiple final oxidized Cu_4O_4 states. Thus, a great diversity of reaction profiles for the attack of supported Cu cluster by O_2 emerges due to the dynamic effects. The kinetics of oxidation reactions catalyzed by the studied Cu oxide clusters would be non-trivially affected by these dynamics, and it is clear that the MEP brings limited information. Dynamics, similar to the one uncovered in this study, would be characteristic of the oxidation of every thermally-populated isomer of the reduced cluster.

ACKNOWLEDGMENTS

This work was funded by DOE-BES grant DE-SC0019152. This work used computational and storage resources of the National Energy Research Scientific Computing Center (NERSC), a U.S. Department of Energy Office of Science User Facility operated under Contract No. DE-AC02-05CH11231. An award of computer time was provided by the Innovative and Novel Computational Impact on Theory and Experiment (INCITE) program. This research used resources of the Argonne Leadership Computing Facility, which is a DOE Office of Science User Facility supported under Contract DE-AC02-06CH11357.

[Supporting Information. Further methods detail; additional figures and tables including surface-cluster model agreement, further minimum energy paths, free energy path, RMSD plots of structural change due to reactant-cluster coupling; and references.](#)

REFERENCES

- (1) Carrero, C. A.; Schloegl, R.; Wachs, I. E.; Schomaeyer, R. Critical Literature Review of the Kinetics for the Oxidative Dehydrogenation of Propane over Well-Defined Supported Vanadium Oxide Catalysts. *ACS Catalysis* **2014**, 4 (10), 3357–3380. <https://doi.org/10.1021/cs5003417>.
- (2) Chen, K.; Bell, A. T.; Iglesia, E. Kinetics and Mechanism of Oxidative Dehydrogenation of Propane on Vanadium, Molybdenum, and Tungsten Oxides. *Journal of Physical Chemistry B* **2000**, 104 (6), 1292–1299. <https://doi.org/10.1021/jp9933875>.
- (3) Tyo, E. C.; Yin, C.; Di Vece, M.; Qian, Q.; Kwon, G.; Lee, S.; Lee, B.; Debartolo, J. E.; Seifert, S.; Winans, R. E.; Si, R.; Ricks, B.; Goergen, S.; Rutter, M.; Zugic, B.; Flytzani-Stephanopoulos, M.; Wang, Z. W.; Palmer, R. E.; Neurock, M.; Vajda, S. Oxidative Dehydrogenation of Cyclohexane on Cobalt Oxide (Co_3O_4) Nanoparticles: The Effect of Particle Size on Activity and Selectivity. *ACS Catalysis* **2012**, 2 (11), 2409–2423. <https://doi.org/10.1021/cs300479a>.

- (4) Nauert, S. L.; Schax, F.; Limberg, C.; Notestein, J. M. Cyclohexane Oxidative Dehydrogenation over Copper Oxide Catalysts. *Journal of Catalysis* **2016**, *341*, 180–190. <https://doi.org/10.1016/j.jcat.2016.07.002>.
- (5) Sonobe, K.; Tanabe, M.; Yamamoto, K. Enhanced Catalytic Performance of Subnano Copper Oxide Particles. *ACS Nano* **2020**, *14* (2), 1804–1810. <https://doi.org/10.1021/acsnano.9b07582>.
- (6) Fukuda, R.; Sakai, S.; Takagi, N.; Matsui, M.; Ehara, M.; Hosokawa, S.; Tanaka, T.; Sakaki, S. Mechanism of NO-CO Reaction over Highly Dispersed Cuprous Oxide on γ -Alumina Catalyst Using a Metal-Support Interfacial Site in the Presence of Oxygen: Similarities to and Differences from Biological Systems. *Catalysis Science and Technology* **2018**, *8* (15), 3833–3845. <https://doi.org/10.1039/c8cy00080h>.
- (7) Yin, G.; Nishikawa, M.; Nosaka, Y.; Srinivasan, N.; Atarashi, D.; Sakai, E.; Miyauchi, M. Photocatalytic Carbon Dioxide Reduction by Copper Oxide Nanocluster-Grafted Niobate Nanosheets. *ACS Nano* **2015**, *9* (2), 2111–2119. <https://doi.org/10.1021/nn507429e>.
- (8) Halder, A.; Ha, M. A.; Zhai, H.; Yang, B.; Pellin, M. J.; Seifert, S.; Alexandrova, A. N.; Vajda, S. Oxidative Dehydrogenation of Cyclohexane by Cu vs Pd Clusters: Selectivity Control by Specific Cluster Dynamics. *ChemCatChem* **2020**, *12* (5), 1307–1315. <https://doi.org/10.1002/cctc.201901795>.
- (9) Poreddy, R.; Engelbrekt, C.; Riisager, A. Copper Oxide as Efficient Catalyst for Oxidative Dehydrogenation of Alcohols with Air. *Catalysis Science and Technology* **2015**, *5* (4), 2467–2477. <https://doi.org/10.1039/c4cy01622j>.
- (10) Li, G.; Zandkarimi, B.; Cass, A. C.; Gorey, T. J.; Allen, B. J.; Alexandrova, A. N.; Anderson, S. L. Sn-Modification of Pt7/Alumina Model Catalysts: Suppression of Carbon Deposition and Enhanced Thermal Stability. *J. Chem. Phys* **2020**, *152*, 024702.
- (11) Zhang, Z.; Zandkarimi, B.; Alexandrova, A. N. Ensembles of Metastable States Govern Heterogeneous Catalysis on Dynamic Interfaces. *Accounts of Chemical Research* **2020**, *53*, 447–458. <https://doi.org/10.1021/acs.accounts.9b00531>.
- (12) Sun, G.; Alexandrova, A. N.; Sautet, P. Structural Rearrangements of Subnanometer Cu Oxide Clusters Govern Catalytic Oxidation. *ACS Catalysis* **2020**, *10* (9), 5309–5317. <https://doi.org/10.1021/acscatal.0c00824>.
- (13) Sun, G.; Alexandrova, A. N.; Sautet, P. Pt8 Cluster on Alumina under a Pressure of Hydrogen: Support-Dependent Reconstruction from First-Principles Global Optimization. *J. Chem. Phys.* **2019**, *151*, 194703. <https://doi.org/10.1063/1.5129296>.
- (14) Sun, G.; Sautet, P. Metastable Structures in Cluster Catalysis from First-Principles: Structural Ensemble in Reaction Conditions and Metastability Triggered Reactivity. *Journal of the American Chemical Society* **2018**, *140* (8), 2812–2820. <https://doi.org/10.1021/jacs.7b11239>.
- (15) Zhai, H.; Alexandrova, A. N. Local Fluxionality of Surface-Deposited Cluster Catalysts: The Case of Pt7 on Al2O3. *Journal of Physical Chemistry Letters* **2018**, *9*, 1696–1702. <https://doi.org/10.1021/acs.jpcllett.8b00379>.

- (16) Zhai, H.; Alexandrova, A. N. Fluxionality of Catalytic Clusters: When It Matters and How to Address It. *ACS Catalysis* **2017**, *7*, 1905–1911. <https://doi.org/10.1021/acscatal.6b03243>.
- (17) Baxter, E. T.; Ha, M. A.; Cass, A. C.; Alexandrova, A. N.; Anderson, S. L. Ethylene Dehydrogenation on Pt_{4,7,8} Clusters on Al₂O₃: Strong Cluster Size Dependence Linked to Preferred Catalyst Morphologies. *ACS Catalysis* **2017**, *7* (5), 3322–3335. <https://doi.org/10.1021/acscatal.7b00409>.
- (18) Ha, M. A.; Baxter, E. T.; Cass, A. C.; Anderson, S. L.; Alexandrova, A. N. Boron Switch for Selectivity of Catalytic Dehydrogenation on Size-Selected Pt Clusters on Al₂O₃. *Journal of the American Chemical Society* **2017**, *139* (33), 11568–11575. <https://doi.org/10.1021/jacs.7b05894>.
- (19) Zhai, H.; Alexandrova, A. N. Ensemble-Average Representation of Pt Clusters in Conditions of Catalysis Accessed through GPU Accelerated Deep Neural Network Fitting Global Optimization. *Journal of Chemical Theory and Computation* **2016**, *12*, 6213–6226. <https://doi.org/10.1021/acs.jctc.6b00994>.
- (20) Groß, A.; Dianat, A. Hydrogen Dissociation Dynamics on Precovered Pd Surfaces: Langmuir Is Still Right. *Physical Review Letters* **2007**, *98* (20), 206107. <https://doi.org/10.1103/PhysRevLett.98.206107>.
- (21) Wang, H.; Miyajima, K.; Kudoh, S.; Mafuné, F. Effect of Atomicity on the Oxidation of Cationic Copper Clusters Studied Using Thermal Desorption Spectrometry. *Physical Chemistry Chemical Physics* **2019**, *21* (41), 23129–23135. <https://doi.org/10.1039/c9cp03892b>.
- (22) Fernández, E.; Boronat, M.; Corma, A. Trends in the Reactivity of Molecular O₂ with Copper Clusters: Influence of Size and Shape. *Journal of Physical Chemistry C* **2015**, *119* (34), 19832–19846. <https://doi.org/10.1021/acs.jpcc.5b05023>.
- (23) Iyemperumal, S. K.; Fenton, T. G.; Gillingham, S. L.; Carl, A. D.; Grimm, R. L.; Li, G.; Deskins, N. A. The Stability and Oxidation of Supported Atomic-Size Cu Catalysts in Reactive Environments. *Journal of Chemical Physics* **2019**, *151* (5), 054702. <https://doi.org/10.1063/1.5110300>.
- (24) Kang, L.; Wang, B.; Bing, Q.; Zalibera, M.; Büchel, R.; Xu, R.; Wang, Q.; Liu, Y.; Gianolio, D.; Tang, C. C.; Gibson, E. K.; Danaie, M.; Allen, C.; Wu, K.; Marlow, S.; Sun, L. dong; He, Q.; Guan, S.; Savitsky, A.; Velasco-Vélez, J. J.; Callison, J.; Kay, C. W. M.; Pratsinis, S. E.; Lubitz, W.; Liu, J. yao; Wang, F. R. Adsorption and Activation of Molecular Oxygen over Atomic Copper(I/II) Site on Ceria. *Nature Communications* **2020**, *11* (4008), 17852. <https://doi.org/10.1038/s41467-020-17852-8>.
- (25) Yu, X.; Zhao, C.; Zhang, T.; Liu, Z. Molecular and Dissociative O₂ Adsorption on the Cu₂O(111) Surface. *Physical Chemistry Chemical Physics* **2018**, *20* (31), 20352–20362. <https://doi.org/10.1039/c8cp03035a>.
- (26) Montemore, M. M.; Van Spronsen, M. A.; Madix, R. J.; Friend, C. M. O₂ Activation by Metal Surfaces: Implications for Bonding and Reactivity on Heterogeneous Catalysts. *Chemical Reviews* **2018**, *118* (5), 2816–2862. <https://doi.org/10.1021/acs.chemrev.7b00217>.

- (27) Diao, Z. Y.; Han, L. L.; Wang, Z. X.; Dong, C. C. The Adsorption and Dissociation of O₂ on Cu Low-Index Surfaces. *Journal of Physical Chemistry B* **2005**, *109* (12), 5739–5745. <https://doi.org/10.1021/jp0457803>.
- (28) Liem, S. Y.; Clarke, J. H. R.; Kresse, G. Pathways to Dissociation of O₂ on Cu(110) Surface: First Principles Simulations. *Surface Science* **2000**, *459* (1), 104–114. [https://doi.org/10.1016/S0039-6028\(00\)00451-9](https://doi.org/10.1016/S0039-6028(00)00451-9).
- (29) Sun, S.; Li, C.; Zhang, D.; Wang, Y. Density Functional Theory Study of the Adsorption and Dissociation of O₂ on CuO(1 1 1) Surface. *Applied Surface Science* **2015**, *333*, 229–234. <https://doi.org/10.1016/j.apsusc.2015.02.018>.
- (30) Xu, Y.; Mavrikakis, M. Adsorption and Dissociation of O₂ on Cu(111): Thermochemistry, Reaction Barrier and the Effect of Strain. *Applied Surface Science* **2001**, *494*, 131–144. <https://doi.org/10.1016/j.apsusc.2016.02.035>.
- (31) Füchsel, G.; Zhou, X.; Jiang, B.; Juaristi, J. I.; Alducin, M.; Guo, H.; Kroes, G. J. Reactive and Nonreactive Scattering of HCl from Au(111): An Ab Initio Molecular Dynamics Study. *Journal of Physical Chemistry C* **2019**, *123* (4), 2287–2299. <https://doi.org/10.1021/acs.jpcc.8b10686>.
- (32) Zhou, L.; Jiang, B.; Alducin, M.; Guo, H. Communication: Fingerprints of Reaction Mechanisms in Product Distributions: Eley-Rideal-Type Reactions between D and CD₃/Cu(111). *Journal of Chemical Physics* **2018**, *149* (3), 031101. <https://doi.org/10.1063/1.5039749>.
- (33) Migliorini, D.; Chadwick, H.; Nattino, F.; Gutiérrez-González, A.; Dombrowski, E.; High, E. A.; Guo, H.; Utz, A. L.; Jackson, B.; Beck, R. D.; Kroes, G. J. Surface Reaction Barriometry: Methane Dissociation on Flat and Stepped Transition-Metal Surfaces. *Journal of Physical Chemistry Letters* **2017**, *8*, 4177–4182. <https://doi.org/10.1021/acs.jpcclett.7b01905>.
- (34) Zhou, X.; Kolb, B.; Luo, X.; Guo, H.; Jiang, B. Ab Initio Molecular Dynamics Study of Dissociative Chemisorption and Scattering of CO₂ on Ni(100): Reactivity, Energy Transfer, Steering Dynamics, and Lattice Effects. *Journal of Physical Chemistry C* **2017**, *121* (10), 5594–5602. <https://doi.org/10.1021/acs.jpcc.6b12686>.
- (35) Jiang, B.; Yang, M.; Xie, D.; Guo, H. Quantum Dynamics of Polyatomic Dissociative Chemisorption on Transition Metal Surfaces: Mode Specificity and Bond Selectivity. *Chemical Society Reviews* **2016**, *45* (13), 3621–3640. <https://doi.org/10.1039/c5cs00360a>.
- (36) Kolb, B.; Guo, H. Communication: Energy Transfer and Reaction Dynamics for DCl Scattering on Au(111): An Ab Initio Molecular Dynamics Study. *Journal of Chemical Physics* **2016**, *145* (1), 011102. <https://doi.org/10.1063/1.4956453>.
- (37) Nattino, F.; Ueta, H.; Chadwick, H.; Van Reijzen, M. E.; Beck, R. D.; Jackson, B.; Van Hemert, M. C.; Kroes, G. J. Ab Initio Molecular Dynamics Calculations versus Quantum-State-Resolved Experiments on CHD₃ + Pt(111): New Insights into a Prototypical Gas-Surface Reaction. *Journal of Physical Chemistry Letters* **2014**, *5* (8), 1294–1299. <https://doi.org/10.1021/jz500233n>.
- (38) Cheng, L.; Yin, C.; Mehmood, F.; Liu, B.; Greeley, J.; Lee, S.; Lee, B.; Seifert, S.; Winans, R. E.; Teschner, D.; Schlögl, R.; Vajda, S.; Curtiss, L. A. Reaction Mechanism for Direct Propylene

Epoxidation by Alumina-Supported Silver Aggregates: The Role of the Particle/Support Interface. *ACS Catalysis* **2014**, 4 (1), 32–39. <https://doi.org/10.1021/cs4009368>.

- (39) Kresse, G.; Joubert, D. From Ultrasoft Pseudopotentials to the Projector Augmented-Wave Method. *Physical Review B* **1999**, 59 (3), 1758–1775. <https://doi.org/10.1103/PhysRevB.59.1758>.
- (40) Kresse, G.; Furthmüller, J. Efficiency of Ab-Initio Total Energy Calculations for Metals and Semiconductors Using a Plane-Wave Basis Set. *Computational Materials Science* **1996**, 6 (1), 15–50. [https://doi.org/10.1016/0927-0256\(96\)00008-0](https://doi.org/10.1016/0927-0256(96)00008-0).
- (41) Kresse, G.; Furthmüller, J. Efficient Iterative Schemes for Ab Initio Total-Energy Calculations Using a Plane-Wave Basis Set. *Physical Review B: Condens. Matter Mater. Phys.* **1996**, 54 (16), 11169–11186. <https://doi.org/10.1103/PhysRevB.54.11169>.
- (42) Kresse, G.; Hafner, J. Ab Initio Molecular-Dynamics Simulation of the Liquid-Metal–Amorphous-Semiconductor Transition in Germanium. *Physical Review B: Condens. Matter Mater. Phys.* **1994**, 49 (20), 14251–14269. <https://doi.org/10.1103/PhysRevB.49.14251>.
- (43) Kresse, G.; Hafner, J. Ab Initio Molecular Dynamics for Liquid Metals. *Physical Review B: Condens. Matter Mater. Phys.* **1993**, 47 (1), 558–561. <https://doi.org/10.1103/PhysRevB.47.558>.
- (44) Blöchl, P. E. Projector Augmented-Wave Method. *Physical Review B* **1994**, 50 (24), 17953–17979. <https://doi.org/10.1103/PhysRevB.50.17953>.
- (45) Perdew, J. P.; Burke, K.; Ernzerhof, M. Generalized Gradient Approximation Made Simple. *Physical Review Letters* **1996**, 77 (18), 3865–3868. <https://doi.org/10.1103/PhysRevLett.77.3865>.
- (46) Dudarev, S.; Botton, G. Electron-Energy-Loss Spectra and the Structural Stability of Nickel Oxide: An LSDA+U Study. *Physical Review B - Condensed Matter and Materials Physics* **1998**, 57 (3), 1505–1509. <https://doi.org/10.1103/PhysRevB.57.1505>.
- (47) Henkelman, G.; Uberuaga, B. P.; Jónsson, H. Climbing Image Nudged Elastic Band Method for Finding Saddle Points and Minimum Energy Paths. *Journal of Chemical Physics* **2000**, 113 (22), 9901–9904. <https://doi.org/10.1063/1.1329672>.
- (48) Henkelman, G.; Jónsson, H. Improved Tangent Estimate in the Nudged Elastic Band Method for Finding Minimum Energy Paths and Saddle Points. *Journal of Chemical Physics* **2000**, 113 (22), 9978–9985. <https://doi.org/10.1063/1.1323224>.
- (49) Lourderaj, U.; Park, K.; Hase, W. L. *Classical Trajectory Simulations of Post-Transition State Dynamics*; 2008; Vol. 27. <https://doi.org/10.1080/01442350802045446>.
- (50) Cho, Y. J.; Linde, S. R. Vande; Zhu, L.; Hase, W. L. Trajectory Studies of SN2 Nucleophilic Substitution . II. Nonstatistical Central Barrier Recrossing in the Cl- + CH3Cl System. *Journal of Chemical Physics* **1992**, 96 (11), 8275–8287.
- (51) Chapman, S.; Bunker, D. L. An Exploratory Study of Reactant Vibrational Effects in CH3+H2 and Its Isotopic Variants. *The Journal of Chemical Physics* **1975**, 62 (7), 2890–2899. <https://doi.org/10.1063/1.430827>.

- (52) Feng, Y.; Zhou, L.; Wan, Q.; Lin, S.; Guo, H. Selective Hydrogenation of 1,3-Butadiene Catalyzed by a Single Pd Atom Anchored on Graphene: The Importance of Dynamics. *Chemical Science* **2018**, 9 (27), 5890–5896. <https://doi.org/10.1039/c8sc00776d>.

TOC Graphics:

